Quantitative Mapping of Scleral Fiber Orientation in Normal Rat Eyes

Michaël J. A. Girard,[1] *Annegret Dahlmann-Noor,*[2] *Sauparnika Rayapureddi,*[2] *Jean Antoine Bechara,*[3] *Benedicte M. E. Bertin,*[4] *Hannah Jones,*[5,6] *Julie Albon,*[5,6] *Peng T. Khaw,*[2] *and C. Ross Ethier*[1]

Purpose. Previous work has suggested a major role of scleral biomechanics in the pathogenesis of glaucoma. Since fiber orientation in connective tissues is a key determinant of tissue biomechanics, experimental characterization of scleral fiber orientation is needed to fully understand scleral biomechanics. This is a report of baseline experimental measurements of fiber orientation in whole normal rat scleras.

Methods. Twenty ostensibly normal Norway brown rat eyes were fixed in 4% paraformaldehyde. The scleras were cleaned of intra- and extraorbital tissues and dissected into five patches, and each patch was glycerol treated to maximize its transparency. Fiber orientation was measured using small-angle light scattering (SALS). Scattering patterns were analyzed to extract two microstructural parameters at each measurement location—the preferred fiber orientation and the degree of alignment—yielding a fiber orientation map for each sclera.

Results. Rat sclera is structurally anisotropic with several consistent features. At the limbus, fibers were highly aligned and organized primarily into a distinct ring surrounding the cornea. In the equatorial region, the fibers were primarily meridionally aligned. In the posterior and peripapillary region, the scleral fibers were mostly circumferential but less aligned than those in the anterior and equatorial regions.

Conclusions. Circumferential scleral fibers may act as reinforcing rings to limit corneal and optic nerve head deformations, whereas equatorial meridional fibers may either provide resistance against extraocular muscle forces or limit globe axial elongation. (*Invest Ophthalmol Vis Sci.* 2011;52:9684–9693) DOI:10.1167/iovs.11-7894

From the [1]Department of Bioengineering, Imperial College, London, United Kingdom; [2]UCL Institute of Ophthalmology and Moorfields Eye Hospital, National Institute for Health Research Biomedical Research Center, London, United Kingdom; [3]Ecole Polytechnique, ParisTech, Palaiseau, France; [4]PHELMA (School of Physics, Applied Physics, Electronics and Materials Science), Institut National Polytechnique de Grenoble, Grenoble, France; and the [5]School of Optometry and Vision Sciences, and [6] CITER (Cardiff Institute of Tissue Engineering and Repair), Cardiff University, Cardiff, Wales, United Kingdom.

Presented in part at the Association for Research in Vision and Ophthalmology annual meeting, Fort Lauderdale, Florida, May 2010.

Supported by The Royal Society, Wolfson's Excellence Award (CRE), the National Institute for Health Research Biomedical Research Center, and the Fight for SightHelen Hamlyn Trust (PTK, SR, AD-N).

Submitted for publication May 17, 2011; revised August 13 and September 25, 2011; accepted October 19, 2011.

Disclosure: **M.J.A. Girard**, None; **A. Dahlmann-Noor**, None; **S. Rayapureddi**, None; **J.A. Bechara**, None; **B.M.E. Bertin**, None; **H. Jones**, None; **J. Albon**, None; **P.T. Khaw**, None; **C.R. Ethier**, None

Corresponding author: C. Ross Ethier, Department of Bioengineering, Imperial College London, South Kensington Campus, London SW7 2AZ, UK; r.ethier@imperial.ac.uk.

Glaucoma is the most common cause of irreversible blindness worldwide.[1] It leads to vision loss by damaging retinal ganglion cell (RGC) axons at the site of the optic nerve head (ONH).[2] The underlying pathogenesis of RGC damage in glaucoma is not fully understood, and hence there are no clinically proven therapies that directly target the process of RGC damage.[3]

Our recent work[4,5–8] and that of others[9–12] have emphasized the potential importance of the sclera in glaucoma. Because the peripapillary sclera surrounds the site of damage in glaucoma (i.e., the ONH), the IOP-induced deformations of the sclera are directly transmitted to ONH tissues. In fact, computational simulations have suggested that the elastic modulus of the sclera is the principal determinant of strain within the ONH.[13] In this context, it is interesting to note that the biomechanical properties of the monkey posterior sclera are altered in both early[14] and moderate[4] stages of glaucoma and with age,[5] suggesting an adaptive remodeling response in this tissue in response to biomechanical load.

If mechanical stretch is a risk factor for RGC damage, as has been widely hypothesized,[15] then factors influencing scleral biomechanics could be important in glaucoma, motivating further studies of the sclera. Scleral strength is conferred primarily by type I collagen fibers[16] formed into an irregular arrangement of multilayered lamellae. Such lamellae are of various thicknesses[17,18] and help resist the mechanical effects of intraocular pressure (IOP). Within each lamella, the collagen fibrils run tangentially to the scleral shell and are oriented in a preferred direction to various degrees.[18] Most previous studies of scleral biomechanics have not explicitly accounted for scleral fiber organization, even though recent computational modeling shows that changing peripapillary scleral fiber orientation (but not stiffness) dramatically influences acute IOP-induced ONH deformations.[19] Accounting for scleral fiber orientation in biomechanical studies requires quantitative information about scleral fiber orientation, but most existing work is qualitative.[20] To our knowledge, only two published studies have mapped fiber orientation in entire scleral shells, using time-consuming histologic reconstructions of cadaveric human eyes.[21,22] Unfortunately, these studies did not provide information on the degree of fiber alignment. A more recent study provided fiber alignment information and reported differences in scleral microstructure between eyes from Caucasian and African-American donors.[11] Although important, this study was restricted to a single region (temporal quadrant) of the peripapillary sclera. Our goal was to quantitatively map whole globe scleral fiber orientation, establishing baseline data in normal (control) rat eyes, as a necessary first step toward applying similar techniques in a rat model of glaucoma. Toward this end, we used an experimental technique known as small-angle light scattering (SALS).

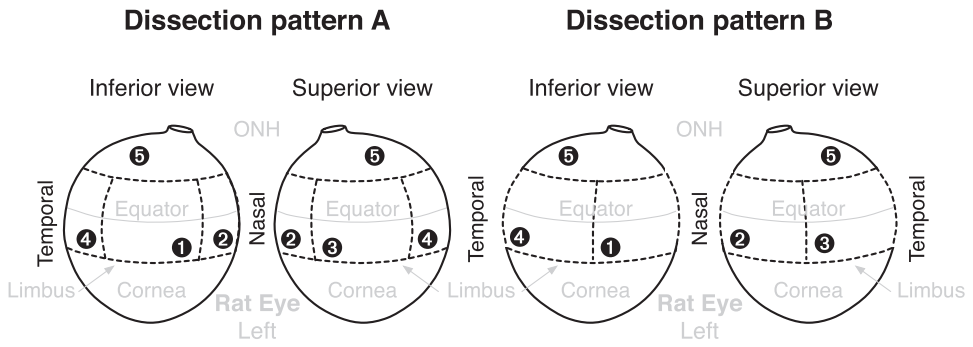

FIGURE 1. Two dissection patterns were used to generate five nearly flat scleral patches for each eye, with *dashed lines* indicating dissection cuts. The eyes were randomly assigned to either dissection pattern. For both dissection patterns, patch 5 contains the ONH near its center, the peripapillary sclera, and part of the posterior sclera. Patches 1 to 4 contain regions of anterior, equatorial, and posterior sclera. For dissection pattern A, the following regionalization was used: 1, inferior; 2, nasal; 3, superior; and 4, temporal, and for dissection pattern B: 1, inferonasal; 2, superonasal; 3, superotemporal; and 4, inferotemporal.

MATERIALS AND METHODS

Experimental Setup and Testing Protocol

Specimen Preparation. All experiments adhered to the ARVO Statement for the Use of Animals in Ophthalmic and Vision Research. Twenty ostensibly normal eyes from young adult Norway brown rats of either sex (two eyes from each of 10 rats) were enucleated and immersion fixed in 4% paraformaldehyde. The scleras were cleaned of intra- and extraorbital tissues and dissected into five nearly flat patches (10 scleras of dissection pattern A and 10 of dissection pattern B, as shown in Fig. 1). We used two dissection patterns because fiber orientation data from the edges of patches are not reliable. By combining fiber orientation data from eyes scanned with these two patterns, we were able to obtain relatively complete measurements over the entire scleral surface. Each patch was then dipped in glycerol solution for several seconds, to slightly enhance the inherent transparency of the sclera,[23] and was laid flat with a drop of glycerol solution between two microscope glass slides (size, 75 × 25 mm), separated by 1-mm-thick double-sided adhesive tape at both extremities. The glass plate assembly was further sealed on all four edges with quick-drying silicone and stored at 4°C for 1 hour (for faster silicone curing) before beginning the experiment.

Small-Angle Light Scattering. Fiber orientation was characterized using SALS[24–29] (Fig. 2). Each glass plate assembly described above was mounted in a custom holder and raster scanned with a 5-mW nonpolarized HeNe laser (model 1125, wavelength: 632.8 μm, and beam diameter, 800 μm; JDS Uniphase, Milpitas, CA) at predetermined locations (>1000 locations per patch, 100 μm linear spacing) using an *x*–*y* translation stage assembly (model NT55-282; Edmund Optics, Barrington, NJ), which was motorized using two linear actuators (model NT58-674; Edmund Optics). A spatial-filter beam-shrinker assembly (modified from KT310/M; Thorlabs, Newton, NJ), which was customized with one focusing and one collimating aspheric lens and a 50-μm pinhole, was positioned between the laser and each specimen to generate a laser beam with a Gaussian intensity profile and a reduced diameter of approximately 500 μm. Note that for SALS applications, a beam diameter higher than 350 μm was found to generate lower noise levels.[24] To ensure that the laser beam was correctly aligned as it passed through the spatial-filter beam-shrinker assembly, two mirrors with dual tilts were used. As the light interacted with each tissue patch, it was scattered by the fibrous tissue proteins (mainly collagen in the case of the sclera) and projected onto a diffuser screen. The diffuser screen contained a blackout beam block in its center to filter unwanted nonscattered light. A CCD camera (resolution: 1024 × 768 pixels, 8–16 bits; model B953; Pixelink, Ottawa, ON, Canada), equipped with a low-distortion/high-resolution lens (NT56-788; Edmund Optics) and a red band-pass filter (model FL632.8-3; Thorlabs) to eliminate ambient light, was positioned behind the diffuser screen to capture an image of the resulting light pattern at each scanned location (Fig. 3). The entire SALS system was automated by using custom-written c++ subroutines, and was able to perform a raster scan with 1000 sample points in 45 minutes. Finally, we note that the rat sclera is thin (<100 μm)[30] and therefore is an ideal tissue to be used with SALS, which works well for tissues less than 500 μm thick.[24]

Interpretation of the Scattered-Light Patterns. To extract fiber organization information from the acquired scattering patterns, it is crucial to interpret them using appropriate optics theory. We opted for a simple (but accurate) approach from among the

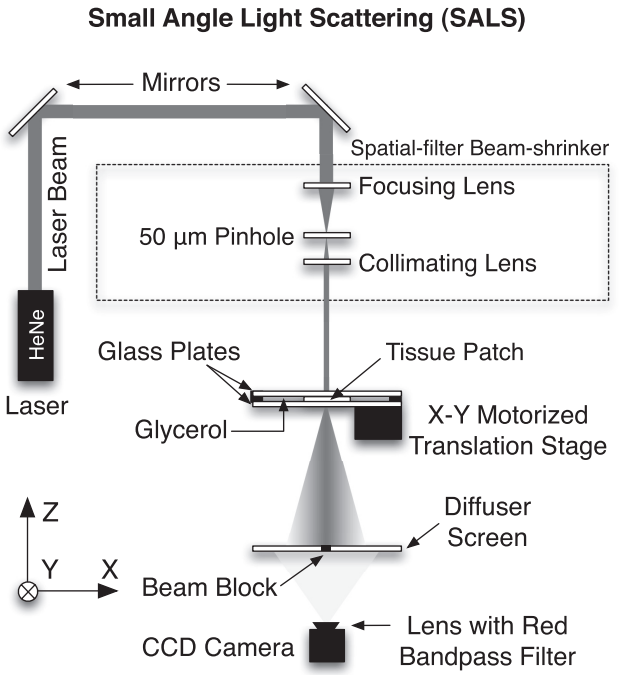

FIGURE 2. The SALS apparatus. After noise removal and beam diameter reduction with a spatial-filter beam-shrinker assembly, laser light interacts with each dissected tissue patch. Light is then scattered owing to the protein fibers (mainly collagen) and projected onto a diffuser screen equipped with blackout material in its center acting as a beam block. A CCD camera equipped with a red band-pass filter to eliminate ambient light takes a snapshot of the resulting scattered-light pattern. HeNe, helium-neon.

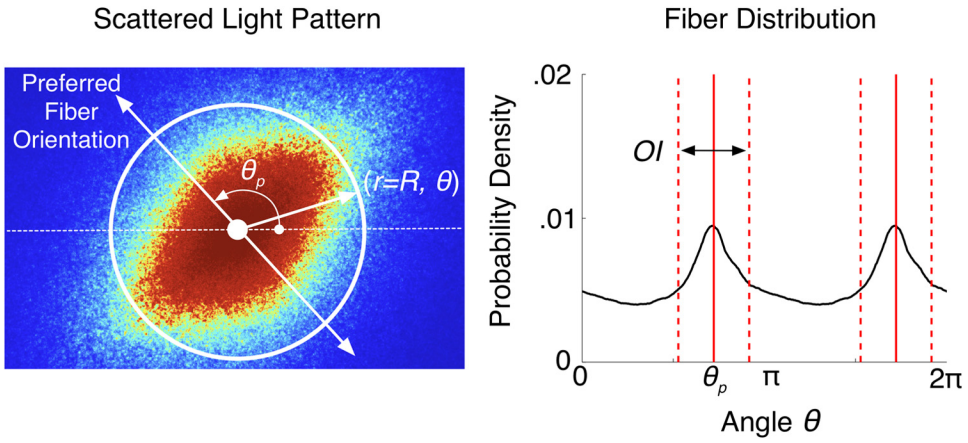

FIGURE 3. Typical small-angle light scattering data pattern at a single tissue location (*left*). For a fiber assembly (or thin soft tissue such as the sclera), the normalized scattered light intensity (a function of the azimuthal angle θ at a fixed radius $r = R$) is the fiber distribution that is sought, but shifted by 90° (*right*). From each fiber distribution, we defined the preferred fiber orientation (modal angle θ_R at the distribution peak) and the orientation index *OI* from which the degree of alignment (0, random alignment or planar isotropy; 1, perfect alignment or transverse isotropy) was computed. Note that each fiber distribution is π-periodic.

numerous possibilities.[31] Using Fraunhofer diffraction theory, it can be shown that the intensity of the scattering pattern produced by a small rectangular aperture (of width a, length b, and angle ϕ defined in the plane of the aperture, which is perpendicular to the laser beam) is[32]

$$I(r,\theta) = I_0^2 \frac{a^2b^2}{\lambda^2L^2} \operatorname{sinc}^2[\pi\bar{a}r \sin(\theta-\phi)]\operatorname{sinc}^2[\pi\bar{b}r \cos(\theta-\phi)], \quad (1)$$

where I is the imaged intensity; r, θ are polar coordinates measured from the center of the scattering pattern; I_0 is the incident light intensity; λ is the laser wavelength; L is the distance between the aperture and the diffuser screen; sinc is the sine cardinal function; and $\bar{a} = a/\lambda L$ and $\bar{b} = b/\lambda L$. We then used Babinet's principle, which states that the scattering pattern of a rectangular aperture is the same (except in its center) as that produced by a fiber (e.g., collagen I) of the same size and shape. Since thin, soft tissues can be considered to be fiber assemblies, and, under the assumption of linearity (as demonstrated in[24] for thin soft tissues), the scattering intensity for a fiber assembly I_{FA} can be obtained from equation 1 as

$$I_{FA}(r,\theta) = I_0^2 \frac{a^2b^2}{\lambda^2L^2} \int_{\theta-\pi/2}^{\theta+\pi/2} P(\theta-\chi)\operatorname{sinc}^2(\pi\bar{a}r \sin\chi)\operatorname{sinc}^2(\pi\bar{b}r \cos\chi)d\chi, \quad (2)$$

where we performed the following change of variable $\chi = \theta - \phi$ for simplicity. For our purposes, the key quantity in equation 2 is P, the fiber distribution function, which describes the angular distribution of fibers responsible for each generated scattered light pattern. In other words, equation 2 tells us that the total scattered-light intensity is the weighted linear sum (through P) of the contribution of each fiber. Finally, under the assumption of high aspect-ratio (i.e., thin and long) fibers, which is satisfied for collagen I, equation 2 can be considerably simplified, as proposed by McGee and coworkers,[32] as

$$I_{FA}(r,\theta) = I_0^2 \underbrace{\frac{a^2b^2}{\lambda^2L^2} \frac{\operatorname{sinc}^2(\pi\bar{a}r)}{\bar{b}r}}_{\text{constant term}} P(\theta - \pi/2). \quad (3)$$

Equation 3 is a simple result, as the term in front of P does not depend on θ and can be regarded as a constant of proportionality. Using the normalization condition for P (i.e., $\int_{-\pi/2}^{+\pi/2} P(\theta)d\theta = 1$),), equation 3 can be simplified to extract P as

$$P(\theta - \pi/2) = \frac{I_{FA}(r,\theta)}{\int_{-\pi/2}^{+\pi/2} I_{FA}(r,\theta)d\theta}. \quad (4)$$

Equation 4 implies that the normalized light intensity distribution at any chosen radius $r = R$ corresponds to that of the fibers, but shifted 90°.

Extraction of Fiber Probability Distributions. Equation 4 is rather elegant and simple and allows the extraction of a fiber distribution for a given scattered-light pattern image with limited digital image processing, as follows. First, the symmetry property of I_{FA} is worth noting.

$$I_{FA}(r,\theta) = I_{FA}(r,\theta + 180°). \quad (5)$$

This symmetry condition was used to define the center of each scattering pattern by minimizing the following function

$$\sum_{i=1}^{n} \left| I_{FA}(r,\theta_i) - I_{FA}(r,\theta_i + 180°) \right|, \quad (6)$$

where $\theta_i \in [\![1°,2°, \ldots ,360°]\!]$, using to a genetic optimization algorithm known as differential evolution.[33] Once obtained, the center of each image was taken as the origin of the polar coordinate system (r,θ). In equation 4, the radius $r = R$ was chosen to be large (i.e., 300 pixels, which corresponds to the image limit) to avoid the effects of the central beam spot. For each angle $\theta_i \in [\![1°,2°, \ldots ,360°]\!]$, $I_{FA}(R,\theta_i)$ was computed from each image by averaging pixel intensity values over a 20 × 20 pixel window centered at (R,θ_i). This step helped reduce noise. $I_{FA}(R,\theta_i)$ was then averaged (to further reduce noise), by using the aforementioned symmetry condition

$$I_{FA}(R,\theta_i) = \frac{I_{FA}(R,\theta_i) + I_{FA}(R,\theta_i + 180°)}{2}, \quad (7)$$

then normalized and finally shifted 90° according to equation 4 to obtain the fiber distribution P.

Microstructural Parameters. From each fiber distribution P, we defined the preferred fiber orientation θ_P to be the mode (peak) of the fiber distribution. We also computed the degree of fiber alignment by first computing the orientation index *OI*, introduced by Sacks et al.[24] and mathematically defined as

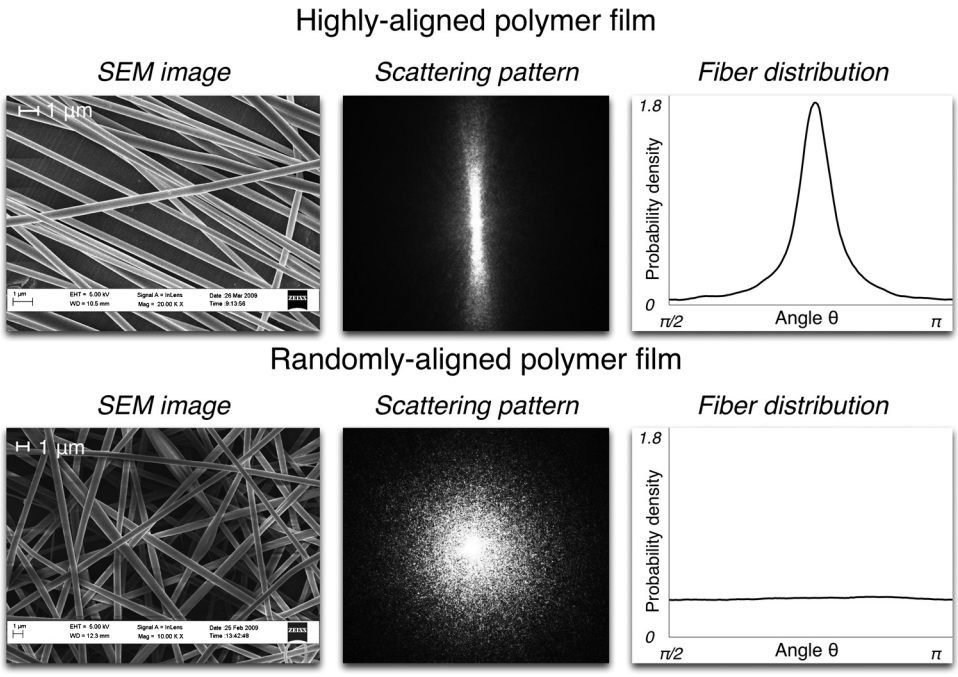

FIGURE 4. SEM images, scattering patterns, and corresponding fiber distributions for highly aligned and randomly aligned polymer films. For the highly aligned polymer film, a von Mises-like distribution was extracted, confirming the high degree of alignment present in the specimen. For the randomly aligned polymer film, the semicircular uniform distribution was obtained, suggesting near-perfect isotropy. These experiments confirm the validity of our SALS system.

$$\int_{\theta_P - OI}^{\theta_P + OI} P(\theta) d\theta = \frac{1}{2}. \quad (8)$$

OI is a measure of fiber spread and represents the length of the interval (in degrees), centered on θ_P, that includes 50% of the total number of fibers (Fig. 3). Based on *OI*, we then defined the degree of alignment as $1 - OI/90°$. This intuitive parameter lies between 0 and 1 and increases with the degree of fiber anisotropy[29]: When it equals 0, the material is planar isotropic (random alignment of the fibers within a plane), whereas when it equals 1, it is transversely isotropic (all fibers aligned in the same direction within the plane of the tissue). Similarly, based on θ_P, we defined the circumferentiality as $1 - \theta_P/90°$. The circumferentiality has a value of 1 if the preferred fiber orientation is parallel to the eye's equator (for scleral patches encompassing the equator) or tangential to the margin of the scleral canal (for scleral patches centered on the ONH) and has a value of 0 if the preferred fiber orientation is instead perpendicular to the equator/scleral canal.

Validation and Sensitivity Analysis

We first validated our experimental protocol, as explained below.

Validation Using Highly and Randomly Aligned Polymer Films. We performed SALS measurements on highly and randomly aligned polymer films (film thickness, 100 μm; film composition, electrospun nanofibers[34]; and fiber thickness, 300–600 nm; Fig. 4). For the randomly aligned polymer film, we obtained a nearly semicircular, uniform distribution, as expected. For the highly aligned polymer film, we obtained a unimodal distribution (von Mises-like) with a large peak value suggesting high alignment. We noticed a slight isotropic contribution in the latter case. This is however not surprising, as the highly aligned polymer films are not perfect and exhibit a certain degree of randomness (see SEM image in Fig. 4). This series of tests confirmed that our SALS experiments and subsequent image analyses were performed properly.

Effect of Tissue Flattening. We investigated how the process of flattening scleral patches (necessary for SALS) may have affected the scleral microstructure. Such effects are difficult to assess experimentally, as a full characterization of scleral patch geometry and corresponding 3-D deformations during flattening would be needed. Therefore, we instead used the finite element method to numerically simulate the scleral-flattening process (software FEBio; Musculoskeletal Research Laboratories, University of Utah, Salt Lake City). To this end, a scleral patch (patch 5; Fig. 1) was digitally reconstructed as an idealized spherical cap (Fig. 5A). The diameter of the sphere was chosen to be 6.40 mm (SD 0.18), which was the averaged axial length of six normal adult rat eyes. The cap covered a third of the eye's axial length according to the dissection patterns described in Figure 1. The spherical cap was modeled as an isotropic elastic solid that could undergo large deformation (St. Venant-Kirchhoff model; Poisson's ratio $\nu = 0.48$; Young's modulus $E = 4$ MPa) and compressed between two rigid bodies to simulate the flattening of the patch between two microscope slides. A penalty method was used to model a sliding, friction-free interface between the spherical cap and the two rigid bodies (penalty factor, 100 MN $\cdot$ m^{-1}; see deformations in Fig. 5A). Using this simulation, we measured the fiber deviation angle (of a virtual fiber, identified by two material points contained within the plane tangential to the patch surface) after flattening. This deviation angle was found to be a function of the distance from the center of the cap (varying from 0 to 2.8 mm) and a function of the initial fiber orientation (0° corresponds to an initial fiber orientation that is radial and 90° to one that is circumferential; Fig. 5B). The maximum fiber deviation angle was found to be 3.82°, and this "error" varied smoothly. This finding suggests that the measured scleral microstructure would be only minimally affected by flattening.

Validation Using Second-Harmonic Imaging. To further validate that our SALS apparatus provided correct fiber orientation measurements for scleral tissue, we employed second-harmonic imaging to image a 100-μm-thick cryosection of a normal bovine ONH. Forward-scattered, second-harmonic generation (SHG) signals were collected by using band-pass filters (380–420 nm) after excitation at 800 nm by a mode-locked Ti:sapphire laser (Chameleon; Coherent UK, Ltd., Ely, UK). Tiled, high-resolution (512 $\times$ 512 pixels) images were acquired with a multiphoton laser scanning electron microscope (SEM) (LSM510 META; Carl Zeiss Meditec, Ltd., Welwyn Garden City, UK) with a motorized stage and fully automated scanning software. On such images, the SHG scatter, depicting collagen in the peripapillary sclera, lamina cribrosa beams, and central retinal blood vessel walls, is pseudocolored green (Fig. 6A). SALS was then employed on the same tissue section to extract a co-localized fiber organization map (100 μm

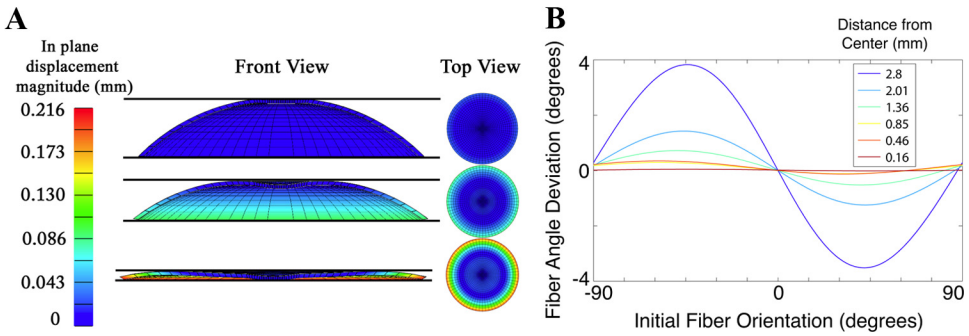

Figure 5. (**A**) Finite element simulation showing the deformed geometry of the scleral patch (reconstructed as a spherical cap to mimic patch 5) at three instants during the flattening process. The in-plane displacement magnitude (horizontal plane) is shown as a color map. For example, larger horizontal displacements (*red*) due to flattening are observed at the edge of the patch. (**B**) The change in fiber angle due to flattening, computed as the difference before and after flattening for fiber contained within the plane tangential to the patch surface. The graph shows this difference as a function of the distance from the center of the cap (0–2.8 mm) and of the initial fiber orientation, where 0° corresponds to an initial fiber orientation that is radial and 90° to one that is circumferential. A maximum fiber angle deviation of 3.82° was found (occurring at the edge of the patch), which suggests that rat scleral fiber orientation is only minimally affected by flattening.

spacing; Fig. 6B). Overall, we found a high level of agreement between the two techniques, where features such as radial laminar beams and circumferential scleral fibers at the scleral canal were observed. This series of tests further confirmed that our SALS experiments and subsequent image analyses were performed correctly for scleral tissue.

Effect of Glycerol Treatment. To verify that the glycerol treatment employed in our experimental protocol did not affect our SALS measurements, we scanned one porcine ONH tissue cryosection (thickness, 30 μm) before and after glycerol treatment of several seconds (Fig. 7). A thin section was used to allow laser light to be scattered, even in the absence of clearing glycerol treatment. Overall, it can be observed that glycerol treatment had only a very minor impact on tissue microstructure.

Data Analysis

For each rat eye, four stripes were defined along the superior, nasal, inferior, and temporal meridians (dissection pattern A), or along the superotemporal, superonasal, inferonasal, and inferotemporal meridians (dissection pattern B). Each stripe was defined as a subset of measurement grid locations and consisted of "rows" of five adjacent measurement points along its width (Fig. 8). We pooled data from corresponding rows over all eyes within a meridian and within a dissection pattern (e.g., all data from the row nearest the limbus in the superior quadrant for dissection pattern A were treated as one pool of 50 points: 5 points/eye times 10 eyes). Similar pooling was performed over each row to give fiber alignment statistics at 100 μm intervals from the limbus (for patches 1–4) or from the edge of the scleral canal (patch 5). The degree of alignment and the circumferentiality were then reported for each pool of data, yielding spatially resolved fiber alignment statistics for all meridians considered in our two dissection schemes.

Results

Maps of scleral fiber organization showed regions of relatively aligned fibers at the limbus and equator and in the peripapillary sclera (Figs. 9, 10), while other locations showed no notable degree of fiber alignment. At the limbus, the fibers were preferentially, although not exclusively, aligned in the circumferential direction, whereas at the equator they were primarily aligned meridionally. A circumferential ring (composed of most but not all the fibers) was clearly observed around the ONH, although the degree of alignment in this peripapillary scleral ring was less than that at the limbus or at the equator.

When data from all eyes were pooled, the degree of alignment was found to exhibit a consistent W shape when plotted

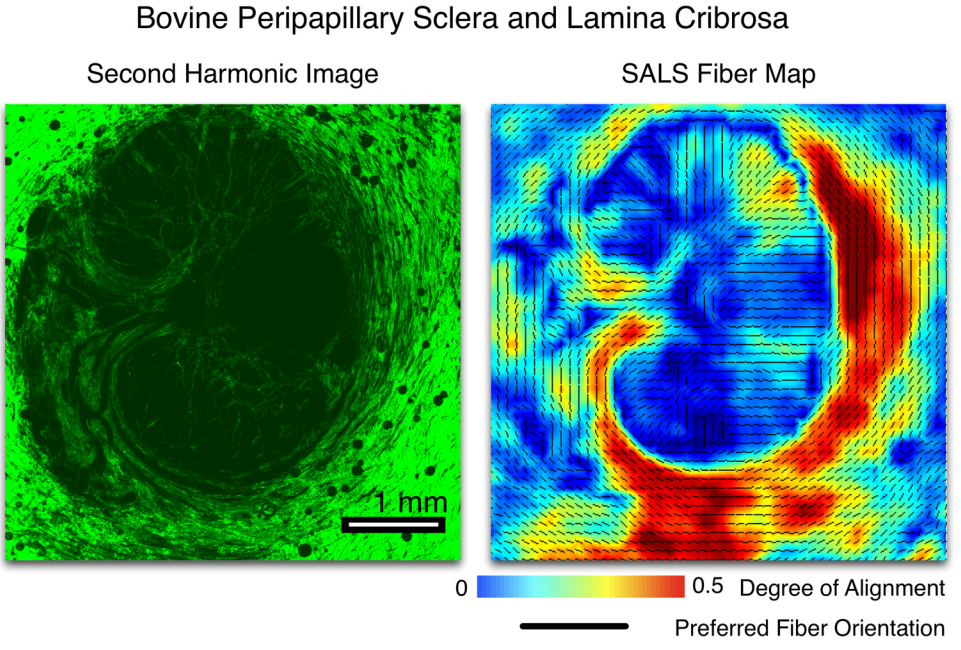

Figure 6. (**A**) Second-harmonic image of a 100-μm-thick bovine ONH tissue section. The SHG signal (identifying the collagenous tissues peripapillary sclera and lamina cribrosa) is pseudocolored *green*. (**B**) Co-localized fiber organization map of the same tissue section obtained using SALS. Colors indicate the degree of alignment (*red* and *blue* correspond to high and low degrees, respectively) and the *black* vectors indicate the preferred fiber orientation. Features such as circumferential fibers at the scleral canal and radial fibers within the lamina cribrosa can be observed in both (**A**) and (**B**), helping to validate the SALS measurements.

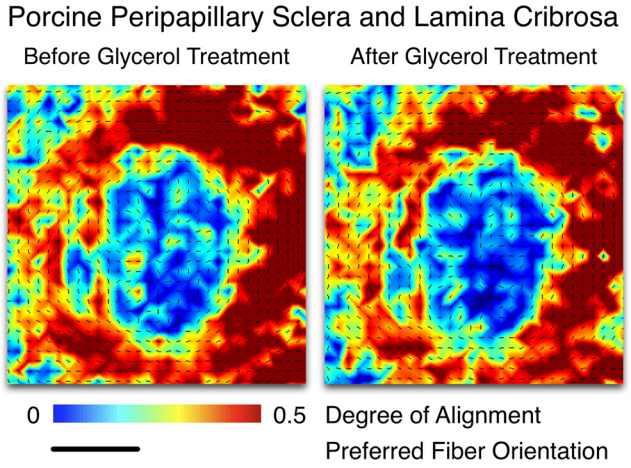

FIGURE 7. Fiber organization maps (before and after glycerol treatment) for one 30-μm-thick porcine ONH section (spacing, 200 μm). Colors indicate the degree of alignment (*red* and *blue* correspond to high and low degrees, respectively) and the *black* vectors indicate the preferred fiber orientation. Features such as circumferential fibers at the scleral canal and radial fibers within the lamina cribrosa are present, as in Figure 6. Overall, it can be observed that glycerol treatment had only a minor impact on tissue microstructure.

versus distance from the limbus (Figs. 11, 12). Local maxima were observed at the limbus, at the equator, and immediately adjacent to the scleral canal, consistent with the individual samples shown in Figures 9 and 10. When the data were pooled over all eyes and all meridians, the degree of alignment (median value) was 0.28 at the limbus (using the row of data closest to the limbus), 0.25 at the equator (using the row of data located 1.8 mm away from the limbus), and 0.16 immediately adjacent to the scleral canal (using the row of data closest to the scleral canal).

Similar plots of circumferentiality versus distance from the limbus exhibited maxima at the limbus and within the peripapillary sclera immediately adjacent to the scleral canal. This trend was consistent for all eight meridians (Figs. 11, 12). When the data were pooled over all eyes and all meridians, the circumferentiality (median value) was 0.93 at the limbus and 0.89 immediately adjacent to the scleral canal. In the equatorial region, the fibers were found to be meridional as indicated by the near-0 circumferentiality values (median, 0.09 over all eyes).

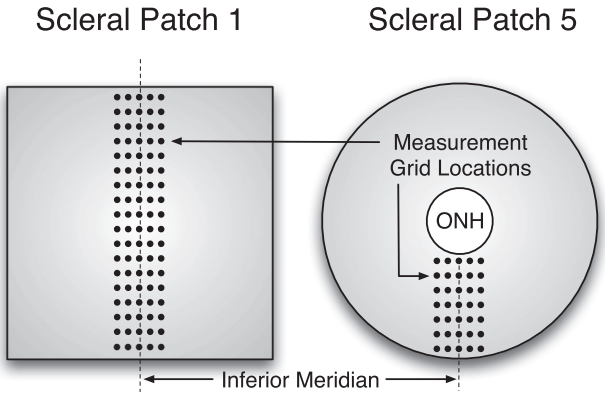

FIGURE 8. Each measurement stripe was defined as a subset of measurement grid locations and consisted of five grid locations widthwise. The stripes are defined for scleral patches 1 and 5 along the inferior meridian. Data were averaged "across the stripe"—that is, over the five grid points perpendicular to the meridional direction. These averaged data were then pooled between eyes, as used to create the plots in Figures 11 and 12.

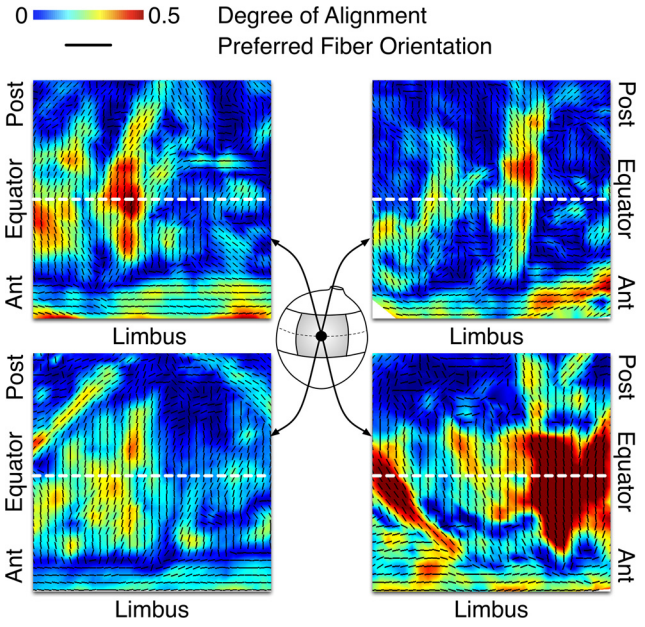

FIGURE 9. Fiber organization maps for the inferior scleral patch from four individual rat eyes. *Colors* indicate the degree of alignment, and *black* bars indicate the preferred fiber orientation. Although large variability was present across all patches, several consistent features were also present. At the limbus, the fibers were highly aligned and organized into a distinct ring (i.e., preferred fiber orientation parallel to the limbus boundary) surrounding the cornea. In the equatorial region, the fibers were primarily meridionally aligned. Post, posterior; Ant, anterior.

DISCUSSION

In this study, we quantitatively assessed and mapped fiber orientation from whole rat scleras to establish baseline data in normal (control) eyes, as the first step toward measuring changes in scleral fiber orientation in eyes with experimental glaucoma. We observed several striking features in the organization of the rat sclera. First, it contains two fiber rings, one at the limbus and the other within the peripapillary sclera, merging with the scleral canal boundary. Second, scleral fibers were preferentially aligned in the meridional direction at the equator.

The presence of a highly aligned fiber ring at the limbus is in agreement with the data reported in humans[35,36] and marmosets,[37] according to small-angle x-ray scattering (SAXS).[38] SALS and SAXS are similar, in that they measure the orientations of fibrous molecules through interaction with radiation: either light (here HeNe laser light; wavelength: 632.8 nm) or x-rays (wavelength: 0.1–10 nm), respectively. Maximum scattering occurs when the fibers have diameters comparable to the probe radiation wavelength; in the case of SAXS, collagen molecules and collagen fibrils[39] are typically the primarily scatterers, whereas in SALS, larger molecules such as collagen fibers and collagen fiber bundles[39] scatter the light. Despite the difference in scattering sources, SALS and SAXS typically lead to similar information on soft tissue microstructure.[40]

The role of the fibrous rings within the rat sclera is almost certainly mechanical. Newton and Meek[35] argued that the limbal fiber ring is present in humans to help prevent corneal deformations and hence maintain proper acuity. Recently, Grytz and coworkers[41] used an elegant computational remod-

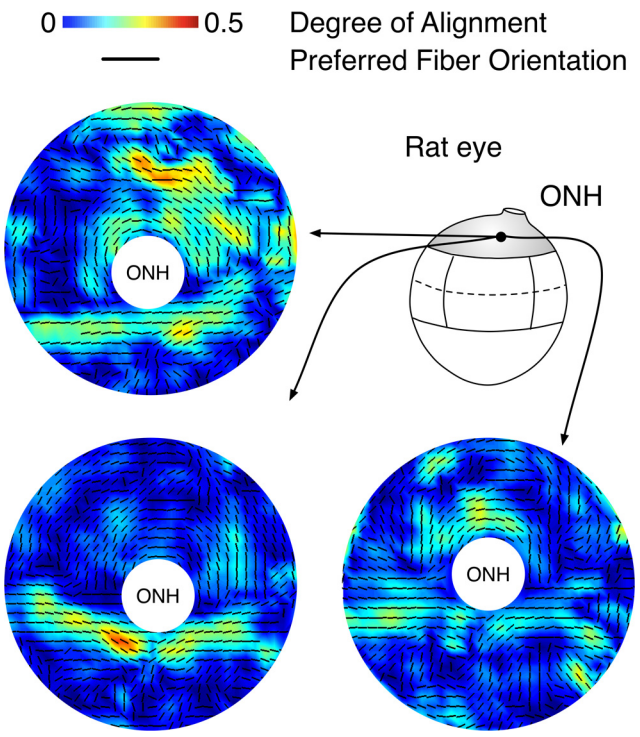

FIGURE 10. Fiber organization maps from three selected scleral patches (peripapillary scleral region surrounding the ONH). Colors indicate the degree of alignment (*red* and *blue* correspond to high and low degrees, respectively) and the *black* vectors indicate the preferred fiber orientation. Although much variability was present across all patches, several consistent features were present. In the peripapillary scleral region, scleral fibers were mostly circumferential (with respect to the scleral canal) but less aligned than those in the anterior and equatorial regions.

eling approach, based on that of Hariton et al.,[42,43] to derive the optimum fiber configuration in an idealized human corneoscleral shell to limit overall mechanical stress. They showed that a limbal fiber ring best limits the large stresses that would otherwise occur at the limbus because of the sudden change in corneoscleral shell curvature. The situation is somewhat more complex in the rat eye, where there is not a substantial change in shell curvature at the limbus (i.e., the rat cornea does not protrude as it normally does in humans but remains largely tangential to the scleral shell at the limbus). However, although we were unable to locate data for rats, it is commonly accepted in other species that the cornea is mechanically weaker than the surrounding sclera.[44] Assuming this to be case in the rat as well, one would expect that circumferential fibers at the limbus would limit pressure-induced limbal stress concentrations where these two tissues of different mechanical properties meet. Such limbal rings may be a common feature of eyes where there are mismatches in either geometry or mechanical properties.

The second ring of collagen fibers in the peripapillary sclera immediately adjacent to the ONH was first documented in human and porcine cadaveric eyes by Kokott[21,22] in the 1930s, and later observed by other investigators through qualitative means (histology) in humans,[20] and mice.[45] Consistent with these observations, computational models have recently shown that a peripapillary fiber ring is the optimum configuration: (1) to match 3-D experimental deformation data of monkey scleral shells[5] and (2) to shield the human lamina cribrosa from high stress.[46]

This study quantifies previous observations. Interestingly, we found that collagen fibers in the peripapillary scleral ring were on average less aligned than those in the limbal ring. This finding may be explained by a recent computational study in which we showed that scleral canal expansion and ONH bowing are inversely related, and their magnitudes can be controlled through the degree of alignment of those fibers surrounding the ONH.[19] In other words, a perfectly aligned peripapillary scleral ring would significantly decrease scleral canal expansion after an acute increase in IOP, but at the cost of substantial bowing of the ONH tissues. It would be interesting to measure peripapillary scleral fiber alignment in glaucomatous eyes, as abnormalities in this structure could alter the biomechanical environment of the ONH.

The second striking feature observed in rat sclera was the presence of highly aligned meridional fibers in the equatorial region (Fig. 9). To our knowledge, such an arrangement has not been reported in any species. To explain this feature, we propose two hypotheses. First, six extraocular muscles insert into the rat sclera (as in humans), and four of them (the rectus muscles) do so in the immediate vicinity of the equatorial sclera.[47,48] Highly aligned meridional fibers at the equator may simply provide resistance against pulling forces from these extraocular muscles. However, since rectus muscle insertions do not cover the whole circumference of the eye (but meridional fibers do as shown herein), this hypothesis can be only partially valid. Alternatively, while circumferential equatorial fibers would allow the whole globe to deform like an ellipsoid,[19] meridional fibers at the equator should help maintain proper acuity by minimizing axial elongation (induced by IOP or otherwise). To verify either hypothesis, one could quantify fiber orientation as a function of depth, as Abahussin et al.[49] did for the corneal stroma. They found that the outer layers of the corneal stroma were structurally anisotropic, whereas the inner layers were isotropic. They suggested that the isotropy from the inner stromal layers sustains the IOP, whereas the anisotropy in the outer layer resists forces from the four rectus muscles attached to the outer sclera in the immediate vicinity of the limbus.

Because of the more random fiber organization in the sclera than in the cornea and the large variations in collagen fiber bundle thickness,[50] the sclera has been proposed to be mechanically isotropic.[51] Our results are consistent with those in the literature that demonstrate that the sclera is structurally anisotropic and can therefore be expected to be mechanically anisotropic. Most computational studies that have investigated the role of ONH and scleral biomechanics in glaucoma have treated the sclera as isotropic. Inclusion of our SALS-derived data in biomechanical models of the eye will improve the predictive capabilities of such models and yield a better understanding of the role of scleral biomechanics in glaucoma.

This study had several limitations. First, SALS, as implemented herein, is a 2-D technique and therefore cannot deduce 3-D fiber arrangements (i.e., it can map only fibers lying within a plane perpendicular to the transmural direction). Fortunately, most fibers lie within this plane for the sclera.[18] However, unlike other thin soft tissues such as skin, the sclera exhibits a certain degree of curvature (a rat eye is approximately 6 mm in diameter), and thus it was necessary to dissect the sclera into multiple patches, which were then laid flat so that the sclera was positioned perpendicular to the laser beam. Overall, we found that the use of five patches was the minimum required to obtain nearly flat scleral patches. Having a patch centered on the ONH allowed us to maintain the integrity of the scleral ring as shown in Figure 10.

Second, to generate the average data in Figures 11 and 12, we assumed that all eyes were of similar size, and measurements were made by using the limbus (scleral patches 1–4) and the scleral canal boundary (scleral patch 5) as references. This assumption could partially explain the large error bars in

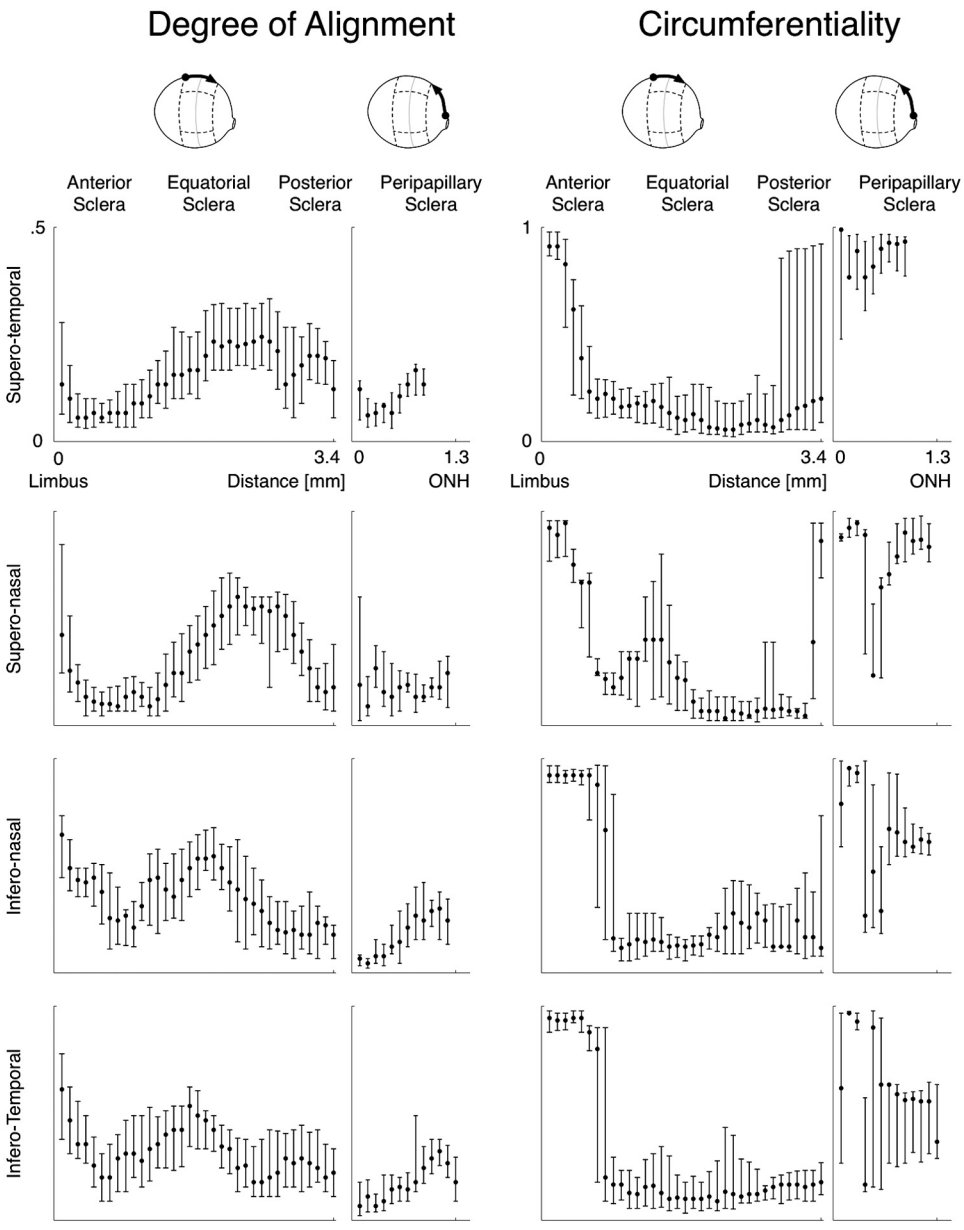

FIGURE 11. The degrees of alignment and circumferentiality were plotted as functions of the distance from the limbus to the scleral canal. Data were pooled for all 10 eyes with dissection pattern B and represented as the 25th, 50th, and 75th percentiles for the superotemporal, superonasal, inferonasal, and inferotemporal meridians. The break in each curve represents the scleral boundary that was cut during dissection where no data could be gathered. For all graphs, the *x*- and *y*-axis scales are the same as those from graphs in the *top* row.

Figures 11 and 12, although they may also reflect normal biological variations in fiber organization (see Figs. 9, 10). In this study, since all eyes were obtained from young adult rats of approximately the same age (3 months), we expected the variations in eye size to be small. We are currently investigating the use of techniques such as optical coherence tomography and microcomputed tomography to provide information about eye size and shape and thus enable better averaging between eyes.

Third, because of the thinness of the rat sclera, we were unable to report fiber orientation measurements as a function of the tissue depth of rat sclera. Other investigators have solved this problem by cutting their samples into thinner subsections. Using this technique, each section can be individually scanned, yielding full-depth fiber orientation information (e.g., with SAXS for the cornea[49] and with SALS for the human sclera).[11] Nevertheless, relying on averaged through-thickness measurements as performed here should not compromise our ability to detect microstructural changes, if any, between normal and glaucomatous rat eyes.

Fourth, our numerical simulation to investigate the effects of flattening on scleral microstructure employed an isotropic elastic model. Since rat sclera is structurally anisotropic in some areas as shown herein, the maximum fiber angle deviation after flattening could be different (smaller or larger) from the 3.82° that we computed.

Finally, it is possible that the act of fixation itself may subtly alter scleral microstructure. We would simply note that fixing whole globes, as we have done, should provide tissue samples that suitably reflect the in situ microstructural arrangement of the sclera. Further, changes due to fixation have not been reported in any previous SALS study that we are aware of.

Acknowledgments

The authors thank the Small-Angle Scattering community (http://scripts.iucr.org/mailman/listinfo/sa_scat) for providing valuable suggestions and Molly Stevens and Yixiang Dong for providing the randomly aligned and highly aligned polymer films that were used to validate the SALS apparatus.

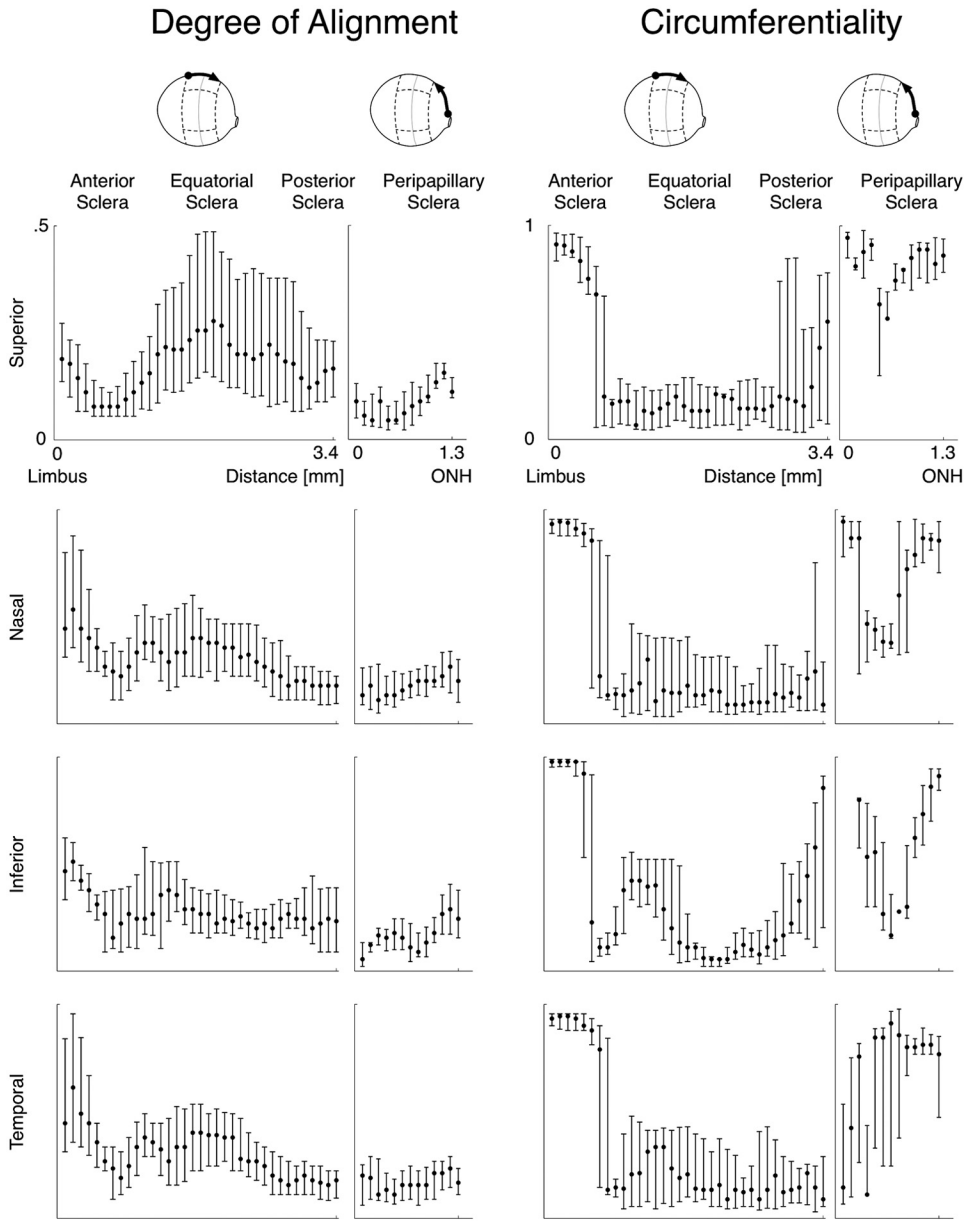

FIGURE 12. The degrees of alignment and circumferentiality were plotted as functions of the distance from the limbus to the scleral canal. Data were pooled for all 10 eyes with dissection pattern A and represented as the 25th, 50th, and 75th percentiles for the superior, nasal, inferior, and temporal meridians. The break in each curve represents the scleral boundary that was cut during dissection where no data could be gathered. For all graphs, the *x*- and *y*-axis scales are the same as those from the graphs in the *top* row.

References

1. Resnikoff S, Pascolini D, Etya'ale D, et al. Global data on visual impairment in the year 2002. *Bull World Health Organ.* 2004;82:844–851.
2. Quigley HA, Addicks EM, Green WR, Maumenee AE. Optic nerve damage in human glaucoma, II: the site of injury and susceptibility to damage. *Arch Ophthalmol.* 1981;99:635–649.
3. Kobelt G. Health economics, economic evaluation, and glaucoma. *J Glaucoma.* 2002;11:531–539.
4. Girard MJ, Suh JK, Bottlang M, Burgoyne CF, Downs JC. Biomechanical changes in the sclera of monkey eyes exposed to chronic IOP elevations. *Invest Ophthalmol Vis Sci.* 2011;52:5656–5669.
5. Girard MJ, Suh JK, Bottlang M, Burgoyne CF, Downs JC. Scleral biomechanics in the aging monkey eye. *Invest Ophthalmol Vis Sci.* 2009;50:5226–5237.
6. Sigal IA, Flanagan JG, Tertinegg I, Ethier CR. Modeling individual-specific human optic nerve head biomechanics, Part II: influence of material properties. *Biomech Model Mechanobiol.* 2009;8:99–109.
7. Norman RE, Flanagan JG, Sigal IA, Rausch SM, Tertinegg I, Ethier CR. Finite element modeling of the human sclera: influence on optic nerve head biomechanics and connections with glaucoma. *Exp Eye Res.* 2011;93:4–12.
8. Eilaghi A, Flanagan JG, Tertinegg I, et al. Biaxial mechanical testing of human sclera. *J Biomech.* 2010;43:1696–1701.
9. Myers KM, Cone FE, Quigley HA, Gelman S, Pease ME, Nguyen TD. The in vitro inflation response of mouse sclera. *Exp Eye Res.* 2010;91:866–875.
10. Myers KM, Coudrillier B, Boyce BL, Nguyen TD. The inflation response of the posterior bovine sclera. *Acta Biomater.* 2010;6:4327–4335.
11. Yan D, McPheeters S, Johnson G, Utzinger U, Vande Geest JP. Microstructural differences in the human posterior sclera as a function of age and race. *Invest Ophthalmol Vis Sci.* 2011;52:821–829.
12. Thornton IL, Dupps WJ, Roy AS, Krueger RR. Biomechanical effects of intraocular pressure elevation on optic nerve/lamina cribrosa before and after peripapillary scleral collagen cross-linking. *Invest Ophthalmol Vis Sci.* 2009;50:1227–1233.
13. Sigal IA, Flanagan JG, Ethier CR. Factors influencing optic nerve head biomechanics. *Invest Ophthalmol Vis Sci.* 2005;46:4189–4199.

14. Downs JC, Suh JK, Thomas KA, Bellezza AJ, Hart RT, Burgoyne CF. Viscoelastic material properties of the peripapillary sclera in normal and early-glaucoma monkey eyes. *Invest Ophthalmol Vis Sci.* 2005;46:540–546.
15. Burgoyne CF, Downs JC, Bellezza AJ, Suh JK, Hart RT. The optic nerve head as a biomechanical structure: a new paradigm for understanding the role of IOP-related stress and strain in the pathophysiology of glaucomatous optic nerve head damage. *Prog Retin Eye Res.* 2005;24:39–73.
16. Edelhauser HF, Ubels JL. The cornea and the sclera. *Adler's Physiology of the Eye*, *Clinical Applications.* St Louis: Mosby; 2003.
17. Rada JA, Shelton S, Norton TT. The sclera and myopia. *Exp Eye Res.* 2006;82:185–200.
18. Watson PG, Young RD. Scleral structure, organisation and disease: a review. *Exp Eye Res.* 2004;78:609–623.
19. Girard MJ, Downs JC, Burgoyne CF, Suh JK. Peripapillary and posterior scleral mechanics, Part I: development of an anisotropic hyperelastic constitutive model. *J Biomech Eng.* 2009;131: 051011.
20. Hernandez MR, Luo XX, Igoe F, Neufeld AH. Extracellular matrix of the human lamina cribrosa. *Am J Ophthalmol.* 1987;104:567–576.
21. Kokott W. Das spaltlinienbild der sklera. (Ein beitrag zum funktionellen bau der sklera). *Klin Monbl Augenheilkd.* 1934;92:177–185.
22. Kokott W. Über mechanisch-funktionelle Strukturen des Auges. *Graefes Arch Clin Exp Ophthalmol.* 1938;138:424–485.
23. Guo X, Guo Z, Wei H, et al. In vivo comparison of the optical clearing efficacy of optical clearing agents in human skin by quantifying permeability using optical coherence tomography. *Photochem Photobiol.* 2011;87:734–740.
24. Sacks MS, Smith DB, Hiester ED. A small angle light scattering device for planar connective tissue microstructural analysis. *Ann Biomed Eng.* 1997;25:678–689.
25. Kronick PL, Sacks MS. Quantification of vertical-fiber defect in cattle hide by small-angle light scattering. *Connect Tissue Res.* 1991;27:1–13.
26. Chien JCW, Chang EP. Small-angle light scattering of reconstituted collagen. *Macromolecules.* 1972;5:610–617.
27. Ferdman AG, Yannas IV. Scattering of light from histologic sections: a new method for the analysis of connective tissue. *J Invest Dermatol.* 1993;100:710–716.
28. Garton A, Carlsson DJ, Stepaniak RF, Wiles DM. The use of small-angle light-scattering (SALS) to examine the structure of fibers 1. *Textile Res J.* 1979;49:335–342.
29. Joyce EM, Liao J, Schoen FJ, Mayer JE Jr, Sacks MS. Functional collagen fiber architecture of the pulmonary heart valve cusp. *Ann Thorac Surg.* 2009;87:1240–1249.
30. Guo L, Tsatourian V, Luong V, et al. En face optical coherence tomography: a new method to analyse structural changes of the optic nerve head in rat glaucoma. *Br J Ophthalmol.* 2005;89: 1210–1216.
31. van de Hulst HC. *Light Scattering by Small Particles.* Mineola, NY: Dover Publications; 1981.
32. McGee SH, McCullough RL. Characterization of fiber orientation in short-fiber composites. *J Appl Phys.* 1984;55:1394–1403.
33. Price KV, Storn RM, Lampinen JA. *Differential Evolution*: *A Practical Approach to Global Optimization.* Berlin: Springer; 2005.
34. Dong Y, Yong T, Liao S, Chan CK, Stevens MM, Ramakrishna S. Distinctive degradation behaviors of electrospun polyglycolide, poly(DL-lactide-co-glycolide), and poly(L-lactide-co-ε-caprolactone) nanofibers cultured with/without porcine smooth muscle cells. *Tissue Eng Part A.* 2010;16:283–298.
35. Newton RH, Meek KM. Circumcorneal annulus of collagen fibrils in the human limbus. *Invest Ophthalmol Vis Sci.* 1998;39:1125–1134.
36. Aghamohammadzadeh H, Newton RH, Meek KM. X-ray scattering used to map the preferred collagen orientation in the human cornea and limbus. *Structure.* 2004;12:249–256.
37. Boote C, Dennis S, Meek K. Spatial mapping of collagen fibril organisation in primate cornea-an X-ray diffraction investigation. *J Struct Biol.* 2004;146:359–367.
38. Glatter O, Kratky O. *Small Angle X-ray Scattering.* London: Academic Press; 1982:515.
39. Fung YC. *Biomechanics: Mechanical Properties of Living Tissues*. 2nd ed. New York: Springer-Verlag; 1993.
40. Liao J, Yang L, Grashow J, Sacks MS. Molecular orientation of collagen in intact planar connective tissues under biaxial stretch. *Acta Biomater.* 2005;1:45–54.
41. Grytz R, Meschke G. A computational remodeling approach to predict the physiological architecture of the collagen fibril network in corneo-scleral shells. *Biomech Model Mechanobiol.* 2010; 9:225–235.
42. Hariton I, de Botton G, Gasser TC, Holzapfel GA. Stress-driven collagen fiber remodeling in arterial walls. *Biomech Model Mechanobiol.* 2007;6:163–175.
43. Hariton I, deBotton G, Gasser TC, Holzapfel GA. Stress-modulated collagen fiber remodeling in a human carotid bifurcation. *J Theor Biol.* 2007;248:460–470.
44. Woo SL, Kobayashi AS, Schlegel WA, Lawrence C. Nonlinear material properties of intact cornea and sclera. *Exp Eye Res.* 1972; 14:29–39.
45. May CA, Lütjen-Drecoll E. Morphology of the murine optic nerve. *Invest Ophthalmol Vis Sci.* 2002;43:2206–2212.
46. Grytz R, Meschke G, Jonas JB. The collagen fibril architecture in the lamina cribrosa and peripapillary sclera predicted by a computational remodeling approach. *Biomech Model Mechanobiol.* 2011;10(3):371–382.
47. Felder E, Bogdanovich S, Rubinstein NA, Khurana TS. Structural details of rat extraocular muscles and three-dimensional reconstruction of the rat inferior rectus muscle and muscle-pulley interface. *Vision Res.* 2005;45:1945–1955.
48. Khanna S, Porter JD. Evidence for rectus extraocular muscle pulleys in rodents. *Invest Ophthalmol Vis Sci.* 2001;42:1986–1992.
49. Abahussin M, Hayes S, Knox Cartwright NE, et al. 3-D collagen orientation study of the human cornea using X-ray diffraction and femtosecond laser technology. *Invest Ophthalmol Vis Sci.* 2009; 50:5159–5164.
50. Komai Y, Ushiki T. The three-dimensional organization of collagen fibrils in the human cornea and sclera. *Invest Ophthalmol Vis Sci.* 1991;32:2244–2258.
51. Woo SL, Kobayashi AS, Lawrence C, Schlegel WA. Mathematical model of the corneo-scleral shell as applied to intraocular pressure-volume relations and applanation tonometry. *Ann Biomed Eng.* 1972;1:87–98.